Convolution Operation on Pancharatnam-Berry Coding Metasurfaces in Visible Band

Song Luo,[1,4] Zhao Xu,[1] Long Zhang,[1,3,*] Zhengyong Song,[2,†] and Zhanghai Chen[1,‡]

[1] *Department of Physics, College of Physical Science and Technology, Xiamen University, Xiamen 361005, China*
[2] *Institute of Electromagnetics and Acoustics, Xiamen University, Xiamen 361005, China*
[3] *State Key Laboratory of Surface Physics and Department of Physics, Fudan University, Shanghai 200433, China*
[4] *Jiujiang Research Institute of Xiamen University, Jiujiang 332000, China*

(Received 31 December 2022; revised 20 February 2023; accepted 14 March 2023; published 19 May 2023)

Coding metasurfaces bring photonic design into a new era for their convenience in manipulating electromagnetic waves in a programmable way. Different coding patterns can be further convoluted to give rise to nontrivial effects such as multiple beam steering, simultaneous control of surface and space waves, and the integration of multiple functionalities. However, previous experimental works have been limited to low frequencies. Extending convoluted coding metasurfaces to optical frequency can significantly reduce the size of structures, and therefore facilitate their applications in optical circuits. Here, we experimentally demonstrate a Pancharatnam-Berry metasurface designed by convoluting two distinct coding patterns. Such a metasurface exhibits integrated functionalities: the optical spin Hall effect and spin to orbital angular momentum conversion, which are robust over a broad visible band and a wide range of incident angles. Our work represents an important step towards multifunctional coding metasurfaces at optical frequency based on convolution operation.

DOI: 10.1103/PhysRevApplied.19.054065

I. INTRODUCTION

A metasurface, composed of a monolayer of subwavelength meta-atoms, is the two-dimensional (2D) counterpart of a metamaterial [1,2]. The amplitude, phase, polarization, and frequency of the electromagnetic wave front as well as the modes can be manipulated by metasurfaces with precise design [3–9]. Among various types of metasurfaces, the Pancharatnam-Berry (PB) metasurface has attracted particularly intense attention due to their capability to manipulate circularly polarized (CP) waves in an unparalleled manner [10–14]. Employing anisotropic and subwavelength meta-atoms with identical geometric parameters but spatially varying orientations, PB metasurfaces introduce a geometrical phase (PB phase) gradient for local transmitted or reflected CP waves. Based on the PB metasurface, numerous planar optical devices have been demonstrated, such as electromagnetic wave deflectors [15,16], vortex beam generators [17,18], and metalenses [19–21].

Recently, the concepts of coding, digital, and programmable metasurfaces have further promoted the development of metasurfaces [22–24]. By digitally coding meta-atoms with phase sequences, coding metasurfaces simplify the design and optimization procedures, and promote their applications in information science. Many novel phenomena have been realized in different coding metasurfaces, such as anomalous reflection [25,26], random diffusion [27,28], independent CP wave-front manipulations [29], and harmonic wave generations [30,31]. Further integration of metasurfaces through convolution operation offers distinct opportunities to realize desired multifunctional metasurfaces without mutual coupling [32,33].

Up to now, convolution operations on coding metasurfaces have been applied at microwave frequencies, terahertz band, as well as acoustic waves [34–36], and the in-plane size of the device is in the range above millimeters, significantly limiting their application in nanophotonics and compact optoelectronic devices. This can be addressed by extending the coding metasurfaces to optical frequency, which can reduce the size of the device down to micrometer scale [37–39]. Moreover, there are increasing types of novel nanomaterials with resonant energy at optical frequency, such as organics, perovskites, and 2D van der Waals materials, which are waiting to be integrated with coding metasurfaces for novel photonic devices [40–42]. Therefore, the convoluted coding metasurface at visible frequency is of great significance, but has not yet been demonstrated experimentally.

*zhanglong@xmu.edu.cn
†zhysong@xmu.edu.cn
‡zhanghai@xmu.edu.cn

In this paper, we demonstrate an integrated coding metasurface working at visible frequency. The phase pattern of the coding metasurface is obtained by performing a convolution operation on two plasmonic PB metasurfaces, which support the optical spin Hall effect (OSHE) and spin-correlated vortex beam generation, respectively. Therefore, the orbital angular momentum (OAM) is incorporated into the OSHE, and the anomalous reflection of the spin-dependent vortex beam can be achieved in the convoluted pattern. Such a design is realized in a single metasurface with all the parameters optimized for optical frequency. The device is systematically characterized by microspectroscopic measurements where far-field scattering patterns of metasurfaces can be directly mapped out with information about angle, polarization, and phase simultaneously. The device exhibits robust functionalities in a broad visible band and a wide range of incident angles. Our result will facilitate the development of coding metasurfaces at optical frequency and pave a new way for nanophotonic devices with multiple functionalities.

II. DESIGN OF PB CODING METASURFACES

The PB metasurface is an ideal tool for manipulating CP waves. By manipulating the pattern of the meta-atom arrays, PB metasurfaces with different functionalities can be achieved, providing an ideal platform to apply the idea of a coding metasurface [43,44]. In this paper, we focus on a plasmonic PB metasurface working in the reflection manner, as it allows ease of fabrication and works in broad ranges of wavelengths and incident angles.

A schematic of the meta-atom is shown in Fig. 1(a), and it consists of three layers: gold bar on top, SiO_2 spacer in the middle, and gold substrate on the bottom. The CP wave reflected by such an anisotropic meta-atom will obtain an additional geometric phase, which is opposite for light with left circular polarization (LCP) and right circular polarization (RCP). To verify that, we consider linearly polarized (LP) light with normal incidence. The amplitude and phase of the reflected beam as a function of wavelength are plotted in Figs. 1(a) and 1(b), respectively. The responses to LP light with polarization along the x and y axes are plotted by the red solid line and black dashed line, respectively. In such a broad visible band from 600 to 800 nm, the amplitudes of the reflected wave for the two LP light polarizations are almost equivalent, except in the range of plasmonic resonances, as indicated by the dips in Fig. 1(a). Moreover, the phase difference between them is close to 180° in this range, as shown by the blue dotted line in Fig. 1(b). Therefore, the meta-atom works as a half-wave plate in the reflection manner for the incident light. The imperfect phase difference and the unequal amplitudes of the x- and y-polarized light will make an impact on the conversion efficiency of the metasurface [45,46].

In Fig. 1(c), we show that the geometric phase, also known as the PB phase, induced by such a meta-atom for the waves with LCP and RCP are opposite, and the phase difference can be continuously tuned by the orientation of the meta-atom. Such a phase gradient is the key element to manipulate the CP light and can be digitally coded for programmable design of the metasurface. We implement the idea of coding the metasurface in three structures,

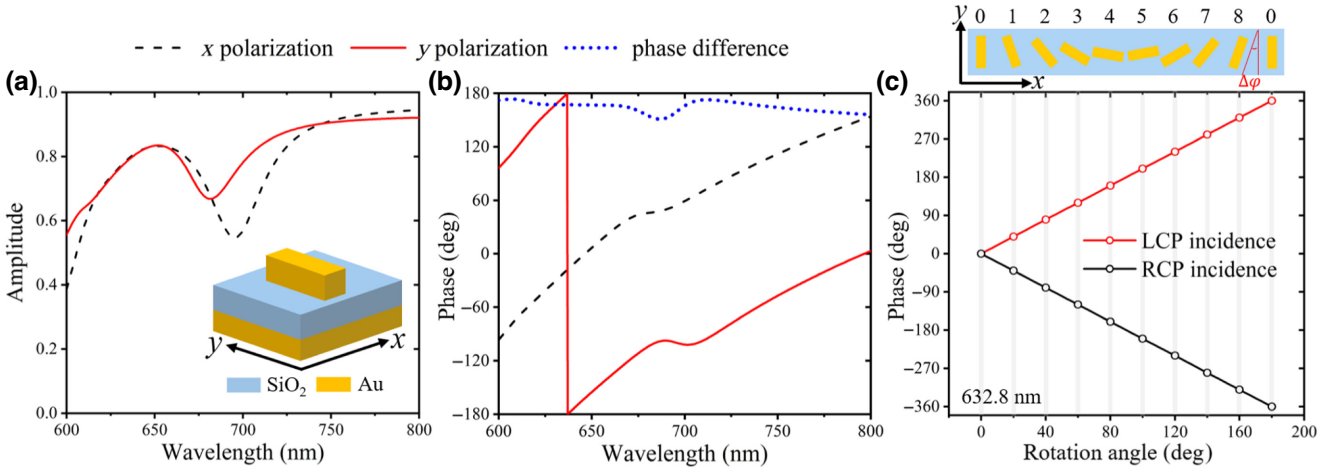

FIG. 1. Simulated normalized amplitude (a) and phase responses (b) of the x- and y-polarized (red solid and black dashed lines) waves reflected from a meta-atom under normal illumination. The inset in (a) is a schematic of the proposed meta-atom. The length, width, and thickness of the top gold bar are 190 nm, 60 nm, and 60 nm, respectively. The thicknesses of SiO_2 film and gold substrate are 70 nm and 100 nm, respectively. The blue dotted line in (b) is the phase difference between x- and y-polarized waves. (c) The phase response versus the rotation angle ($\Delta\varphi$) of the top nanorod of meta-atoms for 632.8 nm with LCP and RCP under normal incidence. The top panel in (c) is a schematic of a supercell, where the lattice constant is 258 nm and the rotation angle $\Delta\varphi$ between adjacent nanorods is 20°.

discussed in the following, where a supercell consists of nine meta-atoms represented by digits from 0 to 8, as shown in the top panel of Fig. 1(c).

III. RESULTS

A. OSHE in a metasurface with linear phase gradient

A PB metasurface with a linear phase gradient shown in Fig. 2(a) can be used to implement the OSHE, referring to transverse splitting of wave vectors of photons with opposite spin. It results from spin-orbit interaction of photons induced by a metasurface, where a spin-dependent refractive index gradient plays the role of a photonic magnetic field [47,48]. A PB metasurface with linear phase gradient covering 2π phase can provide a spin-dependent PB phase to realize the OSHE. According to the generalized Snell's law [49,50], the OSHE can also be understood as an anomalous reflection induced by the PB metasurface, which can be calculated by

$$\sin(\theta_{rx}) = \sin(\theta_{ix}) \pm \frac{2\Delta\varphi}{pk_0}, \tag{1}$$

where θ_{rx} is the reflection angle, θ_{ix} is the incident angle, $k_0 = 2\pi/\lambda$ represents the free-space wave vector, and p is the periodicity of the meta-atom. The phase gradient induced by the metasurface for CP light is $\pm 2\Delta\varphi$, where the positive and negative signs correspond to LCP and RCP, respectively. As indicated by the equation, the shift in

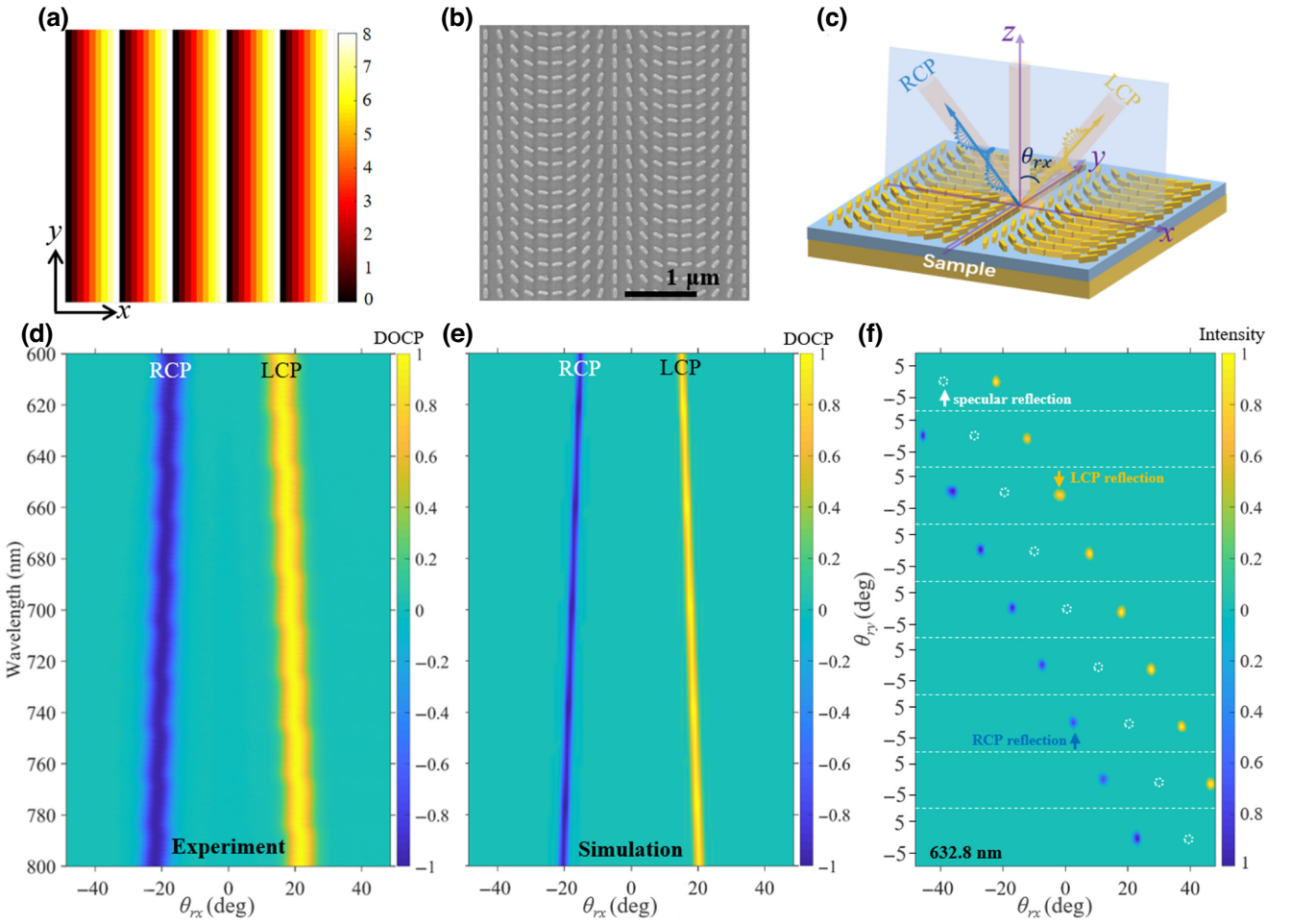

FIG. 2. (a) Linearly periodic gradient phase pattern along the metasurface x direction. The color bar represents the coding number of the phase gradient. (b) SEM image of the fabricated sample. (c) Schematic of the OSHE derived from the linear gradient metasurface and its corresponding coordinate system. (d) The degree of circular polarization (DOCP) of the far-field scattering signal for wavelengths ranging from 600 to 800 nm under normal incidence. (e) The corresponding simulation result. The color bars in (d) and (e) represent the DOCP defined in the main text. (f) Normalized angle-resolved reflection spectrum for 632.8 nm LP laser incidence with different angles. From top to bottom in (f), the incident angles range from -40° to $+40^\circ$. The LCP and RCP reflections are shown on either side of the white dotted circles that represent the specularly reflected plane waves. The color bar represents the normalized intensity of the spectrum. The handedness of the light is denoted by color, with blue and yellow corresponding to RCP and LCP, respectively.

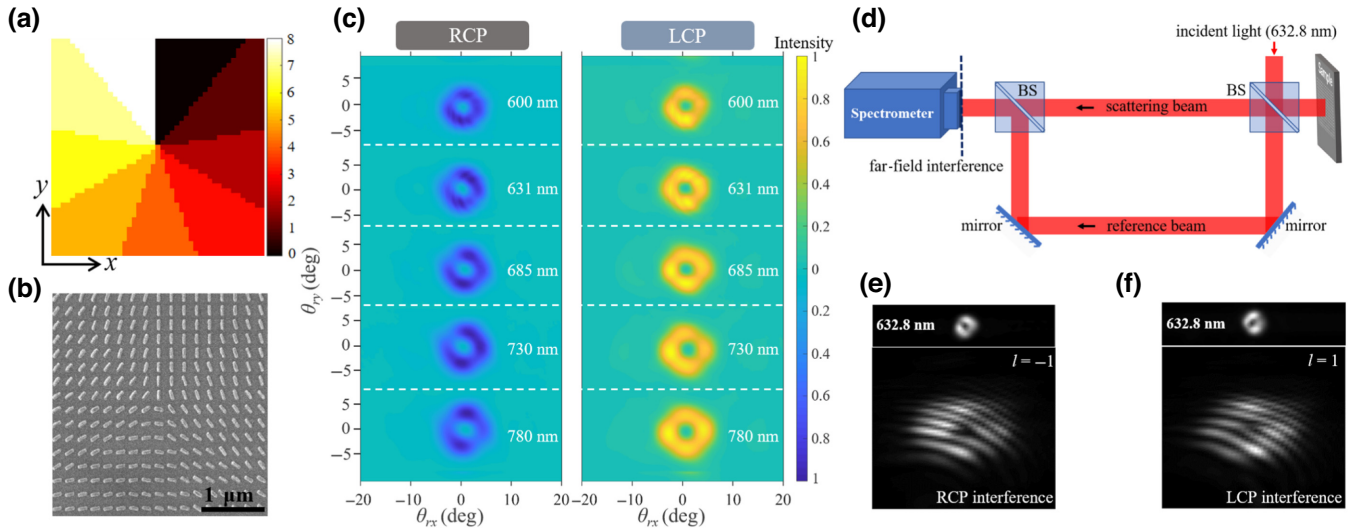

FIG. 3. (a) The spiral-like phase pattern with OAM mode $|l| = 1$. The color bar represents the coding number of the phase gradient. (b) The SEM image of the fabricated sample. (c) Experimental measurements of RCP (left panel) and LCP (right panel) vortex beams generated by the metasurface in panel (b), under normal incidence of LCP (left panel) and RCP (right panel) light at different wavelengths. The color bar represents the normalized intensity of the spectra. The handedness of the vortex beam is denoted by color. (d) Sketch of the interferometric setup. The far-field interference between the scattering beam from the sample and the LP reference beam is detected by the CCD of a spectrometer. (e),(f) The interference patterns of the generated CP vortex beams (top panels) with the LP reference beam of 632.8 nm. The interference patterns around the central hollow of the RCP and LCP vortex beams show forklike fringes with two branches and opposite directions, which reveal that the reflected beams possess OAM of $l = -1$ and $l = 1$, respectively.

direction of the reflected beam can be reversed by changing the handedness of the incident CP light.

Such a digitally coded phase gradient in Fig. 2(a) can be realized by a metasurface, whose SEM image is shown in Fig. 2(b). The OSHE in such a metasurface is verified experimentally with the configuration shown in Fig. 2(c). Under normal incidence of white light that is linearly polarized along the x axis and covers wavelengths from 600 to 800 nm, the reflected light is detected by a home-built spectroscopic setup, where the angle, wavelength, and polarization can be resolved. The DOCP of the reflected light is defined by $(I_{\mathrm{LCP}} - I_{\mathrm{RCP}})/(I_{\mathrm{LCP}} + I_{\mathrm{RCP}})$, where I_{LCP} and I_{RCP} are the intensities of reflected beams with RCP and LCP components measured separately. The DOCP is color coded in Fig. 2(d), with blue and yellow corresponding to RCP and LCP, respectively. The DOCP is close to 100% within the broad band from 600 to 800 nm. The linear dispersion of the reflected beam indicates that the anomalous reflection angle induced by the metasurface is larger for light with longer wavelength, which agrees with Eq. (1).

The experimental result is also well reproduced by the numerical simulation shown in Fig. 2(e). Compared with the simulation, the measured spectrum in Fig. 2(d) exhibits broader linewidth in the dimension of angle, as a result of angular broadening of the incident beam induced by the imperfect collimation of the white light source. Next, we further confirm the robustness of the OSHE over a broad range of incident angles. The wavelength of incident light is fixed at 632.8 nm, and the incident angle of the LP light is tuned in the range between $-40°$ and $40°$. The reflected beam is shown in Fig. 2(f), where the LCP and RCP components are depicted in yellow and blue, respectively. As a reference, the white dotted circles represent the specular reflection of incident light, which is located in the middle of each pair of reflected beams with opposite circular polarizations.

B. Vortex beam generated by a metasurface with spiral-like phase gradient

Vortex beam with OAM can be achieved by rearranging the PB meta-atoms in a spiral-like phase coding sequence. The phase evolution around the propagation direction of a vortex beam can be described by $e^{jl\varphi}$, where l is the topological charge number and φ is the azimuthal angle [51,52]. In general, the generation of a vortex beam can be realized by introducing an azimuth-related helical phase into the optical field. Theoretically, a two-dimensional spiral-like phase distribution can be expressed as [53,54]

$$\Phi(x, y) = l\varphi = l \arctan(y/x), \tag{2}$$

where x and y are the coordinates of meta-atoms along the x and y axes of a metasurface. Accordingly, a spiral-like phase profile on a two-dimensional surface is obtained as

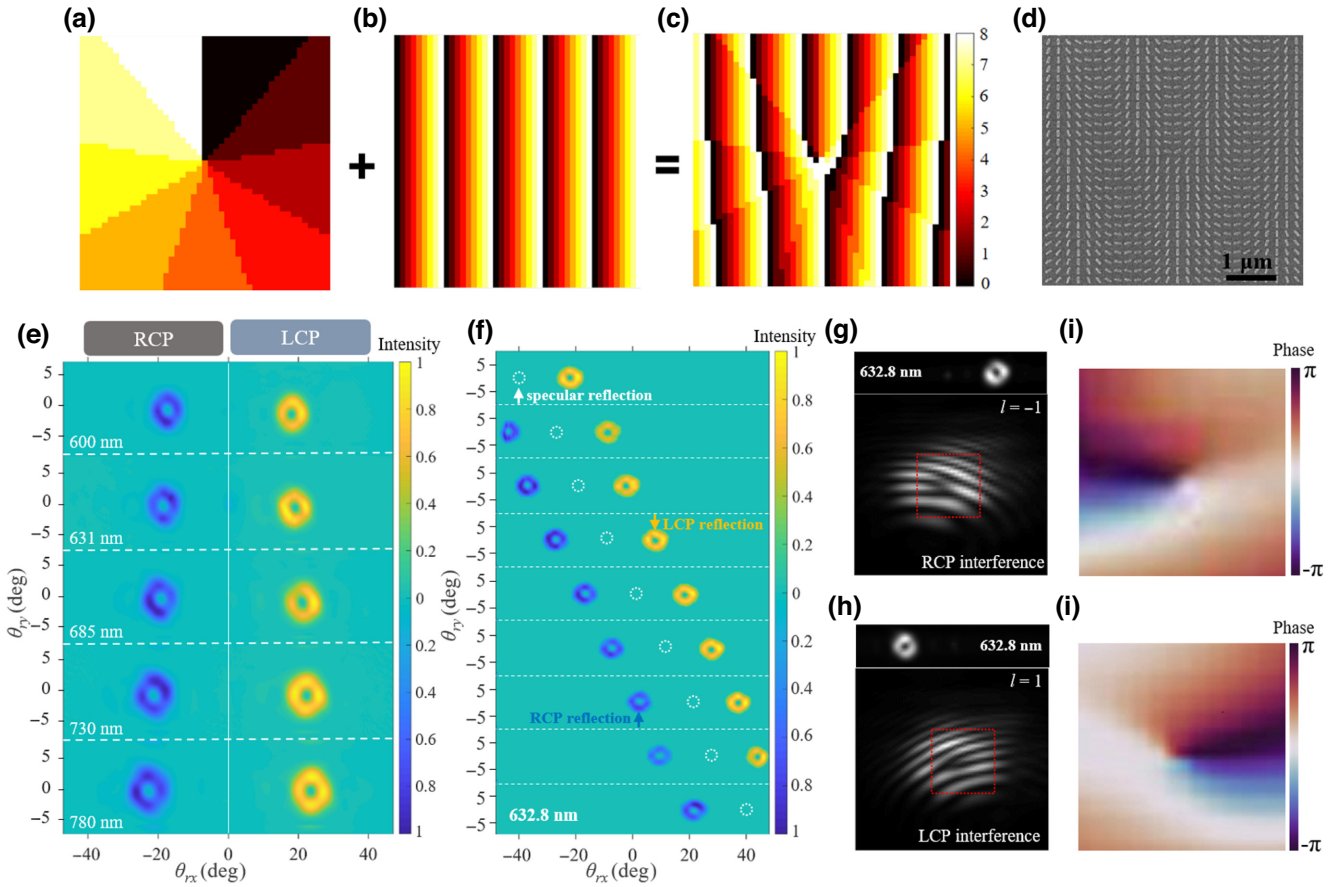

FIG. 4. (a) Coding pattern with OAM mode $|l| = 1$. (b) Coding pattern with linear gradient sequence. (c) Mixed coding pattern formed by superimposing the coding patterns of panels (a) and (b). The color bar represents the coding number of the phase gradient. (d) The SEM image of the convoluted coding metasurface. (e) Experimentally measured RCP (left panel) and LCP (right panel) far-field scattering patterns for LP light with different wavelengths under normal incidence. (f) Normalized angle-resolved reflection spectra for 632.8 nm LP laser incidence with different angles. From top to bottom in panel (f), the incident angles range from -40° to $+40^\circ$. The white dotted circles represent the specularly reflected beams. The color bar represents the normalized intensity of the spectra. The handedness of the light is denoted by color. (g),(h) The interference patterns between the generated CP vortex beams (top panels) and LP reference beam of 632.8 nm. (i),(j) Phase distribution extracted from the two interference patterns in the area marked by the red boxes in panels (g) and (h), respectively. The color bar represents the phase.

shown in Fig. 3(a), which is divided equally into nine sections with constant phase increment $(2\pi/9)$. Similar to the linear phase gradient, such a spiral phase gradient can also be encoded by the digits from 0 to 8, and realized by a metasurface with oriented meta-atoms. Under normal incidence of CP light, the reflected beam will obtain an OAM, i.e., such a PB metasurface will enable the spin selectivity of the OAM.

We fabricate such a metasurface designed at optical frequency, as shown with the SEM image in Fig. 3(b). We characterize the device by sending CP light vertically to the metasurface and detecting the reflected light beam. As shown in Fig. 3(c), the wavelength of the incident beam varies from 600 to 800 nm and the two CP components are detected separately. The reflected beams show a typical ring-shaped profile with a hollow in the center, indicating the generation of vortex beams. In order to further characterize the OAM carried by the reflected light, a far-field interference experiment is carried out between the vortex beam and the reference beam with LP, as schematically shown in Fig. 3(d). The interference patterns are presented in Figs. 3(e) and 3(f), where the two branches of fork fringes with opposite directions are formed near the centers of the vortex beams, indicating that the OAM carried by the LCP and RCP vortex beams are $+\hbar$ and $-\hbar$, respectively.

C. Convolution operation on two coding metasurfaces

The above two PB metasurfaces demonstrate flexible manipulation of the electromagnetic field in the visible band with different degrees of freedom, where linear momentum and OAM are coupled with spin angular momentum (SAM) of the photon in the first and second

devices, respectively. By combining the functionalities of both metasurfaces, all tuning degrees of freedom will be integrated into a single metasurface. This can be realized by performing a convolution operation on the coding patterns of the two metasurfaces, as we show in the following discussion.

It is well known that the far-field scattering pattern of a metasurface ($f(\sin\theta)$) can be deduced by Fourier transforming its near-field coding pattern ($f(x_\lambda)$) [55], i.e.,

$$f(x_\lambda) \overset{\text{FFT}}{\Longleftrightarrow} f(\sin\theta), \tag{3}$$

where $x_\lambda = x/\lambda$ is the electric length and θ is the angle with respect to the normal direction. According to the convolution theorem, such a Fourier transform relationship also applies to the superposition of two scattering patterns, i.e.,

$$f(x_\lambda)\cdot g(x_\lambda) \overset{\text{FFT}}{\Longleftrightarrow} f(\sin\theta) * g(\sin\theta), \tag{4}$$

where the convolution of two scattering patterns in the far field ($f(\sin\theta) * g(\sin\theta)$) can be obtained by Fourier transforming their near-field correspondence: multiplication of the field distribution in real space ($f(x_\lambda)\cdot g(x_\lambda)$). Considering the exponential relationship between the field distribution and phase, the phase pattern of the designed metasurface can be obtained just by adding up the phase of the individual structures, as shown in Figs. 4(a)–4(c). The new phase profile not only inherits the spiral-like phase gradient, but also varies linearly in the x direction. Such a phase gradient can be realized in the fabricated metasurface shown in Fig. 4(d). As a result, spin-dependent anomalous reflection of the vortex beam is expected in this new metasurface.

Figure 4(e) shows the far-field scattering patterns under normal incidence of LP light at different wavelengths. The left and right CP components are resolved experimentally and depicted in different color scales (blue, RCP; yellow, LCP). The spin dependence of the reflection angle and the linear dispersion indicate that the OSHE is inherited. The robustness over a wide range of incident angles is shown in Fig. 4(f) for a fixed wavelength of 632.8 nm. In addition to the OSHE, the ring-shaped intensity profile indicates that the reflected beam carries an additional OAM, which is further confirmed by the interference measurements. As shown in Figs. 4(g)–4(j), the fork pattern with two branches and the extracted phase of the ring-shaped beam demonstrate unambiguously that the reflected beams in opposite directions carry opposite OAM with topological charges -1 and $+1$. Therefore, a coding metasurface with two functionalities is demonstrated by a convolution operation on two distinct metasurfaces, which can be used to generate spin-dependent vortex beams and realize their anomalous reflection (or OSHE). Moreover, such a device still remains robust over a broad visible band and a wide range of incident angles.

D. CONCLUSION

In summary, we numerically and experimentally present three PB coding metasurfaces operating in the visible band, which exhibit robust functionality over a broad range of wave frequencies and incident angles. As a proof of concept, a third metasurface is designed by performing a convolution operation on the coding patterns of the other two. Accordingly, two functionalities are integrated in a single pattern, where the OSHE incorporated with OAM of light is observed. The combination of SAM to OAM conversion, broad visible band, and compactness renders this coding metasurface very attractive for application in both classical physics and quantum sciences at optical frequency [56]. New emerging materials such as 2D semiconductors and perovskites can be readily integrated with the coding metasurfaces in the visible band for novel fundamental concepts and device applications.

ACKNOWLEDGMENTS

This work is supported by National Natural Science Foundation of China under Grants No. 62175207 and No. 11974294, State Key Laboratory of Surface Physics and Department of Physics at Fudan University under Grant No. KF2021_06, Fundamental Research Funds for the Central Universities under Grants No. 20720210004 and No. 20720200074, and China Postdoctoral Science Foundation under Grant No. 2021M691890.

Song Luo and Zhao Xu contributed equally to this work.

APPENDIX A: SAMPLE FABRICATION

All designed metasurfaces in this work are fabricated on silicon substrates. To ensure tight adhesion, an ultrathin Cr layer with a thickness of 10 nm is deposited before depositing each gold layer. Then, gold and SiO_2 layers are successively deposited using an electron-beam evaporator. Finally, the top metasurface patterns are defined by electron-beam lithography with subsequent processes of gold deposition and lift-off.

APPENDIX B: OPTICAL MEASUREMENTS

In experiments, reflection spectra are taken using a home-built angle-resolved spectroscopy setup. Samples are placed on the focal plane. The incident light beam is focused onto the sample by an objective with numerical aperture of 0.75, which is also used to collect light scattered by the metasurface. The Fourier plane (far field) at the position of the back focal plane of the objective is imaged onto a CCD camera. The incident light beams with variable wavelengths in Figs. 3 and 4 are generated via narrowband filtering of a supercontinuum laser source.

APPENDIX C: NUMERICAL SIMULATION

In our simulation, the frequency-dependent complex dielectric permittivity of gold is described by the Drude model, $\varepsilon(\omega) = \varepsilon_\infty - \omega_p^2/\omega^2 + i\gamma\omega$ in the visible wavelength range, where the dielectric permittivity ε_∞, plasma frequency ω_p, and collision frequency γ are set to 12, 1.37×10^{16} rad/s, and 1.05×10^{14} s^{-1}, respectively [57–59].

[1] A. V. Kildishev, A. Boltasseva, and V. M. Shalaev, Planar photonics with metasurfaces, Science **339**, 1232009 (2013).

[2] D. M. Lin, P. Y. Fan, E. Hasman, and M. L. Brongersma, Dielectric gradient metasurface optical elements, Science **345**, 298 (2014).

[3] H. T. Chen, A. J. Taylor, and N. F. Yu, A review of metasurfaces: Physics and applications, Rep. Prog. Phys. **79**, 076401 (2016).

[4] S. L. Sun, Q. He, J. M. Hao, S. Y. Xiao, and L. Zhou, Electromagnetic metasurfaces: Physics and applications, Adv. Opt. Photon. **11**, 380 (2019).

[5] Z. L. Deng and G. X. Li, Metasurface optical holography, Mater. Today Phys. **3**, 16 (2017).

[6] F. Ding, A. Pors, and S. I. Bozhevolnyi, Gradient metasurfaces: A review of fundamentals and applications, Rep. Prog. Phys. **81**, 026401 (2018).

[7] M. Tymchenko, J. S. Gomez-Diza, J. Lee, N. Nookala, M. A. Belkin, and A. Alu, Gradient Nonlinear Pancharatnam-Berry Metasurfaces, Phys. Rev. Lett. **115**, 207403 (2015).

[8] Y. Intaravanne, J. Han, R. X. Wang, A. Ma, S. T. Li, S. N. Chen, and X. J. Chen, Phase manipulation-based polarization profile realization and hybrid holograms using geometric metasurface, Adv. Photon. Res. **2**, 2000045 (2021).

[9] Z. W. Zheng, Y. Zhu, J. Y. Duan, M. B. Qin, F. Wu, and S. Y. Xiao, Enhancing Goos-Hanchen shift based on magnetic dipole quasi-bound states in the continuum in all-dielectric metasurfaces, Opt. Express **29**, 29541 (2021).

[10] M. V. Berry, The adiabatic phase and Pancharatnam's phase for polarized light, J. Mod. Opt. **34**, 1401 (1987).

[11] C. Menze, C. Rockstuhl, and F. Lederer, Advanced Jones calculus for the classification of periodic metamaterials, Phys. Rev. A **82**, 053811 (2010).

[12] N. Shitrit, I. Bretner, Y. Gorodetski, V. Kleiner, and E. Hasman, Optical spin Hall effects in plasmonic chains, Nano Lett. **11**, 2038 (2011).

[13] L. L. Huang, X. Z. Chen, B. F. Bai, Q. F. Tan, G. F. Jin, T. Zentgraf, and S. Zhang, Helicity dependent directional surface plasmon polariton excitation using a metasurface with interfacial phase discontinuity, Light Sci. Appl. **2**, e70 (2013).

[14] S. Y. Xiao, F. Zhong, H. Liu, S. N. Zhu, and J. S. Li, Flexible coherent control of plasmonic spin-Hall effect, Nat. Commun. **6**, 8360 (2015).

[15] L. Huang, X. Chen, H. Mühlenbernd, G. Li, B. Bai, Q. Tan, G. Jin, T. Zentgraf, and S. Zhang, Dispersionless phase discontinuities for controlling light propagation, Nano Lett. **12**, 5750 (2012).

[16] H. Xu, S. Ma, X. Ling, X. Zhang, S. Tang, T. Cai, S. Sun, Q. He, and L. Zhou, Deterministic approach to achieve broadband polarization-independent diffusive scatterings based on metasurfaces, ACS Photon. **5**, 1691 (2018).

[17] F. Yue, D. Wen, C. Zhang, B. D. Gerardot, W. Wang, S. Zhang, and X. Chen, Multichannel polarization-controllable superpositions of orbital angular momentum states, Adv. Mater. **29**, 1603838 (2017).

[18] P. Chen, S. Ge, W. Duan, B. Wei, G. Cui, W. Hu, and Y. Lu, Digitalized geometric phases for parallel optical spin and orbital angular momentum encoding, ACS Photon. **4**, 1333 (2017).

[19] R. X. Zheng, R. H. Pan, G. Z. Geng, Q. Jiang, S. Du, L. L. Huang, C. Z. Gu, and J. J. Li, Active multiband varifocal metalenses based on orbital angular momentum division multiplexing, Nat. Commun. **13**, 4292 (2022).

[20] X. Z. Chen, L. L. Huang, H. Mühlenbernd, G. X. Li, B. F. Bai, Q. F. Tan, G. F. Jin, C. W. Qiu, T. Zentgraf, and S. Zhang, Reversible three-dimensional focusing of visible light with ultrathin plasmonic flat lens, Adv. Opt. Mater. **1**, 517 (2013).

[21] X. Z. Chen, L. L. Huang, H. Mühlenbernd, G. X. Li, B. F. Bai, Q. F. Tan, G. F. Jin, C. W. Qiu, S. Zhang, and T. Zentgraf, Dual-polarity plasmonic metalens for visible light, Nat. Commun. **3**, 1198 (2012).

[22] C. Della Giovampaola and N. Engheta, Digital metamaterials, Nat. Mater. **13**, 1115 (2014).

[23] C. J. Cui, M. Q. Qi, X. Wang, J. Zhao, and Q. Chen, Coding metamaterials, digital metamaterials and programmable metamaterials, Light Sci. Appl. **3**, e218 (2014).

[24] Q. Ma, Q. R. Hong, G. D. Bai, H. B. Jing, R. Y. Wu, L. Bao, Q. Cheng, and T. J. Cui, Editing Arbitrarily Linear Polarizations using Programmable Metasurface, Phys. Rev. Appl. **13**, 021003 (2020).

[25] L. H. Gao, Q. Cheng, J. Yang, S. J. Ma, J. Zhao, S. Liu, H. B. Chen, Q. He, W. X. Jiang, H. F. Ma, Q. Y. Wen, L. J. Liang, B. B. Jin, W. W. Liu, L. Zhou, J. Q. Yao, P. H. Wu, and T. J. Cui, Broadband diffusion of terahertz waves by multi-bit coding metasurfaces, Light Sci. Appl. **4**, e324 (2015).

[26] Y. Zhang, H. Cheng, J. G. Tian, and S. Q. Chen, Frequency-Selected Bifunctional Coding Acoustic Metasurfaces, Phys. Rev. Appl. **14**, 064057 (2020).

[27] D. S. Dong, J. Yang, Q. Cheng, J. Zhao, L. H. Gao, S. J. Ma, S. Liu, H. B. Chen, Q. He, W. W. Liu, Z. Y. Fang, L. Zhou, and T. J. Cui, Terahertz broadband low-reflection metasurface by controlling phase distributions, Adv. Opt. Mater. **3**, 1405 (2015).

[28] H. P. Wang, Y. B. Li, H. Li, J. L. Shen, S. Y. Dong, S. Y. Wang, K. N. Qi, Q. Ma, S. Jin, S. J. Li, and T. J. Cui, Intelligent metasurface with frequency recognition for adaptive manipulation of electromagnetic wave, Nanophotonics **11**, 1401 (2022).

[29] G. W. Ding, K. Chen, X. Y. Luo, J. M. Zhao, T Jiang, and Y. J. Feng, Dual-Helicity Decoupled Coding Metasurface for Independent Spin-to-Orbital Angular Momentum Conversion, Phys. Rev. Appl. **11**, 044043 (2019).

[30] C. Zhang, J. Yang, L. X. Yang, J. C. Ke, M. Z. Chen, W. K. Gao, M. Chen, Z. H. Wu, J. F. Chen, Q. Cheng, and T. J. Cui, Convolution operations on time-domain digital

coding metasurface for beam manipulations of harmonics, Nanophotonics **9**, 2771 (2020).
[31] S. R. Wang, M. Z. Chen, J. C. Ke, Q. Cheng, and T. J. Cui, Asynchronous space-time-coding digital metasurface, Adv. Sci **9**, 2200106 (2022).
[32] S. Liu, T. J. Cui, L. Zhang, Q. Xu, Q. Wang, X. Wan, J. Q. Gu, W. X. Tang, M. Q. Qi, J. G. Han, W. L. Zhang, X. Y. Zhou, and Q. Cheng, Convolution operations on coding metasurface to reach flexible and continuous controls of terahertz, Adv. Sci. **3**, 1600156 (2016).
[33] T. J. Cui, S. Liu, and L. L. Li, Information entropy of coding metasurface, Light Sci. Appl. **5**, e16172 (2016).
[34] R. Feng, B. Ratin, J. J. Yi, K. Zhang, X. M. Ding, H. L. Zhang, A. de Lustrac, and S. N. Burokur, Versatile Airy-Beam Generation Using a 1-Bit Coding Programmable Reflective Metasurface, Phys. Rev. Appl. **14**, 014081 (2020).
[35] H. Zhao, C. M. Zhang, J. Y. Guo, S. T. Liu, X. Z. Chen, and Y. Zhang, Metasurface Hologram for Multi-Image Hiding and Seeking, Phys. Rev. Appl. **12**, 054011 (2019).
[36] B. Y. Xie, K. Tang, H. Cheng, Z. Y. Liu, S. Q. Chen, and J. T. Tian, Coding acoustic metasurfaces, Adv. Mater. **29**, 1603507 (2017).
[37] C. Zhang, S. Divitt, Q. B. Fan, W. Q. Zhu, A. Agrawal, Y. Q. Lu, T. Xu, and H. J. Lezec, Low-loss metasurface optics down to the deep ultraviolet region, Light Sci. Appl. **9**, 55 (2020).
[38] G. T. Cao, H. X. Xu, L. M. Zhou, Y. Deng, Y. X. Zeng, S. H. Dong, Q. Zhang, Y. J. Li, H. Yang, Q. H. Song, X. K. Liu, Y. Li, and C. W. Qiu, Infrared metasurface-enabled compact polarization nanodevices, Mater. Today **50**, 499 (2021).
[39] L. G. Yu, Y. B. Fan, Y. J. Wang, C. Zhang, W. H. Yang, Q. H. Song, and S. M. Xiao, Spin angular momentum controlled multifunctional all-dielectric metasurface doublet, Laser Photon. Rev. **14**, 1900324 (2020).
[40] Y. B. Fan, Y. H. Wang, N. Zhang, W. Z. Sun, Y. S. Gao, C. W. Qiu, Q. H. Song, and S. M. Xiao, Resonance-enhanced three-photon luminesce via lead halide perovskite metasurfaces for optical encoding, Nat. Commun. **10**, 2085 (2019).
[41] J. Zhang, H. Zhang, W. X. Yang, K. Chen, X. Z. Wei, Y. J. Feng, R. H. Jin, and W. R. Zhu, Dynamic scattering steering with graphene-based coding metamirror, Adv. Opt. Mater. **8**, 2000683 (2020).
[42] T. Chervy, S. Azzini, E. Lorchat, S. J. Wang, Y. Gorodetski, J. A. Hutchison, S. Berciaud, T. W. Ebbesen, and C. Genet, Room temperature chiral coupling of valley excitons with spin-momentum locked surface plasmons, ACS Photon. **5**, 1281 (2018).
[43] L. Zhang, S. Liu, L. L. Li, and T. J. Cui, Spin-controlled multiple pencil beams and vortex beams with different polarizations generated by Pancharatnam-Berry coding metasurfaces, ACS Appl. Mater. Inter. **9**, 36447 (2017).
[44] Q. Q. Zheng, Y. F. Li, J. Q. Zhang, H. Ma, J. F. Wang, Y. Q. Pang, Y. J. Han, S. Sui, Y. Shen, H. Y. Chen, and S. B. Qu, Wideband, wide-angle coding phase gradient metasurfaces based on Pancharatnam-Berry phase, Sci. Rep. **7**, 43543 (2017).
[45] W. J. Luo, S. Y. Xiao, Q. He, S. L. Sun, and L. Zhou, Photonic spin Hall effect with nearly 100% efficiency, Adv. Opt. Mater. **3**, 1102 (2015).
[46] S. Q. Li, S. H. Dong, S. X. Yi, W. K. Pan, Y. Z. Chen, F. X. Guan, H. J. Guo, Z. Wang, Q. He, L. Zhou, and S. L. Sun, Broadband and high-efficiency spin-polarized wave engineering with PB metasurfaces, Opt. Express **28**, 15601 (2020).
[47] S. A. Wolf, D. D. Awschalom, R. A. Buhrman, J. M. Daughton, S. von Molnar, M. L. Roukes, A. Y. Chtchelkanova, and D. M. Treger, Spintronics: A spin-based electronics vision for the future, Science **294**, 1488 (2001).
[48] J. Wunderlich, B. G. Park, A. C. Irvine, L. P. Zarbo, E. Rozkotova, P. Nemec, V. Novak, J. Sinova, and T. Jungwirth, Spin Hall effect transistor, Science **330**, 1801 (2010).
[49] S. L. Sun, Q. He, S. Y. Xiao, Q. Xu, X. Li, and L. Zhou, Gradient-index meta-surfaces as a bridge linking propagating waves and surface waves, Nat. Mater. **11**, 426 (2012).
[50] N. Yu, P. Genevet, M. A. Kats, F. Aieta, J. P. Tetienne, F. Capasso, and Z. Gaburro, Light propagation with phase discontinuities: Generalized laws of reflection and refraction, Science **334**, 333 (2011).
[51] V. Y. Bazhenov, M. S. Soskin, and M. V. Vasnetsov, Screw dislocations in light wavefronts, J. Mod. Opt. **39**, 985 (1992).
[52] A. M. Yao and M. J. Padgett, Orbital angular momentum: Origins, behavior and applications, Adv. Opt. Photon. **3**, 161 (2011).
[53] E. Karimi, S. A. Schulz, I. D. Leon, H. Qassim, J. Upham, and R. W. Boyd, Generating optical orbital angular momentum at visible wavelengths using a plasmonic metasurface, Light Sci. Appl. **3**, e167 (2014).
[54] K. Zhang, Y. Y. Yuan, X. M. Ding, H. Y. Li, B. Ratin, Q. Wu, J. Liu, S. N. Burokur, and J. B. Tan, Polarization-engineered noninterleaved metasurface for integer and fractional orbital angular momentum multiplexing, Laser Photon. Rev. **15**, 2000351 (2021).
[55] W. K. Cao, C. Zhang, L. T. Wu, K. Q. Guo, J. C. Ke, T. J. Cui, and Q. Cheng, Tunable Acoustic Metasurface for Three-Dimensional Wave Manipulations, Phys. Rev. Appl. **15**, 024026 (2021).
[56] J. Liu, M. Q. Shi, Z. Chen, S. M. Wang, Z. L. Wang, and S. N. Zhu, Quantum photonics based on metasurfaces, Opt.-Electron. Adv. **4**, 200092 (2021).
[57] P. B. Johnson and R. W. Christy, Optical constants of the noble metals, Phys. Rev. B **6**, 4370 (1972).
[58] R. L. Olmon, B. Slovick, T. W. Johnson, D. Shelton, S. H. Oh, G. D. Boreman, and M. B. Raschke, Optical dielectric function of gold, Phys. Rev. B **86**, 235147 (2012).
[59] D. Y. Wang, F. F. Liu, T. Liu, S. L. Sun, Q. He, and L. Zhou, Efficient generation of complex vectorial optical fields with metasurfaces, Light Sci. Appl. **10**, 67 (2021).